

A Modular Deep Learning Pipeline for Galaxy-Scale Strong Gravitational Lens Detection and Modeling

Sandeep Madireddy
 smadireddy@anl.gov
 Argonne National
 Laboratory
 Lemont, IL

Nan Li
 Nan.Li1@nottingham.ac.uk
 University of Nottingham
 Nottingham, United
 Kingdom

Nesar Ramachandra
 nramachandra@anl.gov
 Argonne National
 Laboratory
 Lemont, IL

James Butler
 butlerj@anl.gov
 Argonne National
 Laboratory
 Lemont, IL

Prasanna Balaprakash
 pbalapra@anl.gov
 Argonne National
 Laboratory
 Lemont, IL

Salman Habib
 habib@anl.gov
 Argonne National
 Laboratory
 Lemont, IL

Katrin Heitmann
 heitmann@anl.gov
 Argonne National
 Laboratory
 Lemont, IL

Abstract

Upcoming large astronomical surveys are expected to capture an unprecedented number of strong gravitational lensing systems in the Universe. Deep learning is emerging as a promising practical tool in detection and quantification of these galaxy-scale image distortions. However, absence of large quantities of representative data from current astronomical surveys requires development of robust forward modeling of synthetic lensing images. Using a realistic and unbiased sample of the strong lenses created by using state-of-the-art extragalactic catalogs, we train a modular deep learning pipeline for uncertainty-quantified detection and modeling with intermediate image processing components for denoising and deblending the lensing systems. We demonstrate a higher degree of interpretability and controlled systematics due to domain-specific task modules that are trained with different stages of synthetic image generation. For lens detection and modeling, we obtain semantically meaningful latent spaces that separate classes and provide uncertainty estimates that explain the misclassified images and provide uncertainty bounds on the lens parameters. In addition, we obtain an improved performance—lens detection (classification) improved from 82% with the baseline to 94%, while the lens modeling (regression) accuracy improved by 25% over the baseline model.

Keywords

Strong Gravitational Lensing, Variational information bottleneck, Representation learning, Residual networks, Denoising, Deblending, Uncertainty quantification.

1 Introduction

Gravitational lensing is the phenomenon by which light rays are deflected as they traverse through curved space caused by the presence of massive astrophysical objects. In the present era of precision cosmology, gravitational lensing has become a powerful probe in many areas of astrophysics and cosmology, from stellar to cosmological scales. Galaxy-galaxy strong lensing (GGSL) is a particular case of gravitational lensing in which the background source and foreground lens are both galaxies and the lensing system is sufficient to distort images of sources into arcs or even rings, depending

on the relative angular position of the two objects. Since the discovery of the first GGSL system in 1988 [20], many valuable scientific applications have been realized, such as studying galaxy mass density profiles [29, 44, 46], detecting galaxy substructure [7, 21, 50], measuring cosmological parameters [12, 42, 47], investigating the nature of high redshift galaxies [8, 15, 43], and constraining the properties of self-interacting dark matter candidates [18, 28, 45].

With the capabilities of the next-generation telescopes such as the LSST,¹ and Euclid² the number of known GGSLs is expected to increase by several orders of magnitude [11]. The forthcoming enormous datasets necessitate an analysis of GGSLs by using automated procedures that operate efficiently and reliably, relying on the high uniformity and quality of the datasets. To this end, several algorithms have been developed to detect GGSLs in image data by recognizing arclike features and the presence of Einstein rings [9, 16, 24, 37]. More recently, efforts to automate GGSL-detection have turned to machine learning (ML), in particular deep learning (DL) algorithms, given their strong performance in image recognition tasks. For instance, the strong gravitational lens detection challenge [33] proved the relative success of applying various ML techniques for automated detection of GGSL systems [6, 9, 19, 23, 30, 36, 41] in comparison with traditional feature extraction techniques. Hezaveh et al. [22] and Pearson et al. [39] have shown the feasibility and reliability of utilizing DL to model strong lenses as an efficient alternative to traditional parametric methods. Perreault-Levasseur et al. [40] presented details about estimating the posteriors of constrained lensing parameters by using a DL method; Morningstar et al [34, 35] demonstrated the possibility of utilizing ML and DL techniques to reconstruct source galaxies in GGSLs. However, the preprocessing of the original images, for example, deblending and denoising with ML, are still in their infancy.

In this paper, we address this growing need for automated analysis of GGSLs in two steps. First, we create a dataset of 120,000 simulated images (60,000 GGSLs and 60,000 non-GGSLs) using a catalog of GGSLs and a state-of-the-art semi-analytic catalog of galaxies (cosmoDC2; [27]) into a strong lensing simulation program named PICS [31]. Second, we develop a modular deep learning pipeline for automated lens detection and modeling for GGSLs. It consists of

¹ <https://www.lsst.org/> ² <https://www.euclid-ec.org/>

four modules: denoising, deblending, lens detection, and lens modeling. We adopt deep residual network (ResNet)-based architectures for denoising the original pixelized images and removing the lens light in the deblending module. The lens detection and modeling modules perform classification and regression, respectively, and are modeled by adopting the variational information bottleneck (VIB) framework [4]. The use of VIB in such a context is a key contribution of our work. Although the VIB approach has been used in multiple works [52], its potential is unexplored for real-world science applications where interpretability and generalizability are as important as the accuracy of the model predictions. The VIB model is a critical component of our modular framework for understanding the functionality and robustness of the learning process of each module from the perspective of a domain scientist. We demonstrate that the VIB model outperforms deep residual network models in terms of accuracy using far fewer parameters and is able to learn an interpretable latent space for both lens detection and modeling tasks. The latent space for classification learns a good representation that can separate classes, as well as put more uncertainty on the misclassified images, which match the physical intuition. For regression, we demonstrate that the representation learned by VIB is more amenable to regression tasks than using unsupervised dimension reduction methods, without a significant drop in accuracy. We note that classical probabilistic approaches have been explored to a great extent in the strong lensing community because the observations from telescopes are typically noisy and hence require the use of uncertainty quantification. Deep learning approaches, on the other hand, are increasingly being adopted to studying strong lensing because of their good modeling accuracy. However, they pose interpretability and trust challenges. The VIB is a promising approach in this direction where probabilistic learning is combined with deep learning in a single learnable framework.

We demonstrate that our modular deep learning pipeline provides significant improvement over a nonmodular end-to-end deep learning model, with the former's classification accuracy being 94% as opposed to 82% of the latter. A similar trend was seen for the lens modeling module, where the accuracy improved by 25%. In addition we found that the lens detection module produces a latent space that separates the two classes when tested on the simulation inputs, while showing higher uncertainty around the misclassified images when the output from the deblending module is fed to the classifier.

2 Data Generation

Currently, only a few hundred observed GGSLs are available [49]. This amount of data is insufficient to train and evaluate deep learning models for searching and modeling thousands of GGSLs, a difficulty that is exacerbated by need for training data for denoising and deblending. Therefore, we created a synthetic dataset that includes 60k GGSLs and 60K non-GGSLs. Of these, 54k GGSLs and 54k non-GGSLs are adopted as training data for the pipeline, and the other 12k images are used as test data to quantify the generalization performance of it.

Simulations of GGSLs comprise six steps: (1) create populations of lenses and sources according to the given statistical properties of GGSLs; (2) build mass and light models of foreground lenses; (3) calculate deflection fields of the lenses; (4) construct light profiles

of background source galaxies; (5) run ray-tracing simulations to create strongly lensed images based on the deflection fields and light profile of sources; and (6) stack the lensed images and the foreground images of lenses, and add the telescope noise as well as the point spread function blurring.

The populations of lenses and sources are built upon a catalog of strong lenses [11] (hereafter, Collett15) and a state-of-the-art extragalactic catalog [27]. Collett15 provides the mass models and simple light models of both lens and source galaxies, and cosmoDC2 provides more realistic light profiles of galaxies containing bulges and disks. To create the inputs for our strong lensing simulation program (named PICS) [31] by connecting the mass profiles from Collett15 and light profiles from cosmoDC2, we cross-match the apparent magnitudes, axis ratios, position angles, and redshifts of the galaxies from Collett15 and CosmoDC2. In principle, if we model a lens galaxy as a smooth ellipsoid, the corresponding GGSL can be described completely by using lensing strength, axis ratio, and position angle. To create a balanced dataset, we sample these three parameters following flat distributions [39].

The mass model of an individual lens galaxy is a singular isothermal ellipsoid (SIE) as adopted in Collett15. This model not only is analytically tractable but also has been found to be consistent with models of individual lenses and lens statistics on length scales relevant for strong lensing [14, 17, 26]. Accordingly, the deflection maps can be given by the parameters of the positions, velocity dispersions, axis ratios, position angles, and redshifts of lenses as well as the redshifts of source galaxies, namely, $\{x_1, x_2, \sigma_v, q_l, \phi_l, z_l, z_s\}$. Since $\{x_1, x_2\}$ can be fixed to $\{0, 0\}$ by centering the cutouts at the lens galaxies and the lensing strength (i.e., Einstein radius) can be given by $R_{\text{ein}} = 4\pi(\sigma_v/c)^2 D(z_l, z_s)/D(z_s)$, the parameter array can be simplified as $\{R_{\text{ein}}, q_l, \phi_l\}$. Here, c is the speed of light, and $D(z_l, z_s)$ and $D(z_s)$ are the angular diameter distance from the deflector to the source and from the observer to the source, respectively.

To achieve the corresponding images of the lenses and sources in a given lensing system with $\{R_{\text{ein}}, q_l, \phi_l\}$, we match it to Collett15 with the properties of $\{R_{\text{ein}}, q_l, \phi_l\}$ to find the redshifts, effective radii, and apparent magnitudes in [g,r,i]-bands of lens and source galaxies separately, namely, $\{z_l, R_l^{\text{eff}}, \text{mag}_l^{[g,r,i]}\}$ and $\{z_s, R_s^{\text{eff}}, \text{mag}_s^{[g,r,i]}\}$. By extracting information from cosmoDC2, we include morphological properties of bulges and disks of the galaxies in Collett15. A process of cross-match between $\{z, R^{\text{eff}}, \text{mag}^{[g,r,i]}\}$ of the galaxies in Collett15 and cosmoDC2 is implemented to assign properties of bulges and disks to the corresponding galaxies. Furthermore, the projected positions of sources in the lensing system are randomly chosen in the area where lensing magnifications are larger than 5 on the source plane. Based on the matched information, we first generate strong lensing images without noise and point spread function (PSF) blurring.

Noise and PSF then are used to make the images realistic by utilizing the models of a ground-based telescope from [11, 13]. The noise model is a mix between read noise, which is a Gaussian-like noise, and shot noise, which is a Poisson-like noise that can be calculated according to the flux in the pixelized images. The PSF model is also a Gaussian function with different full width at half maximum in [g, r, i]-bands. Examples of the mock data are shown in Fig. 2. The non-lensing systems are generated in the same

A Modular Deep Learning Pipeline for Galaxy-Scale Strong Gravitational Lens Detection and Modeling

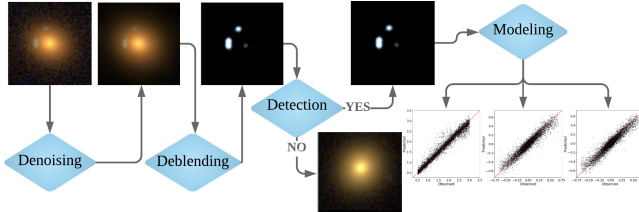


Figure 1: Deep learning pipeline for analysis of galaxy-scale strong lensed systems.

way except that the strong lensing effects have been removed by considering the deflection angles as zeros.

3 Deep Learning Pipeline for Training and Inference

The deep learning pipeline proposed in this work consists of four modules—denoising, source separation (deblending), lens detection (classification), and lens modeling (regression)—as shown in Fig. 1. A typical noisy observation from a telescope would be the input to this pipeline. The denoising module removes the noise without affecting the background galaxy or the foreground lensed light. The denoised images are then passed through the deblending module to remove the foreground lensed light and output the image with just the background galaxy. This background galaxy image is then passed through the lens detection module, which determines whether an image contains a lensed or an unlensed galaxy. All the galaxies that are labeled as lensed are then passed through the lens modeling module to identify its characteristics. A modular framework is necessary for our study because each module by itself is complex enough that it should be separately validated via parametric variations. Moreover, having individual modules is critical for interpretability and incorporating different hierarchies of domain knowledge into each module’s model and training without affecting other modules. We describe below each of the four modules.

3.1 Denoising and Deblending

Denoising is an image restoration approach used to recover a clean image from a noisy observation. Traditionally, image denoising has been posed as an inverse problem, where optimization approaches and special-purpose regularizers (known as image priors) have been used [5]. Recently, deep-learning-based approaches have been increasingly adopted and are emerging as state-of-the-art [32, 53] algorithms for image denoising. We adopt a deep residual network-based enhanced deep super-resolution (EDSR) architecture [32], which was developed for a specific type of image restoration known as super resolution. Since the inputs and the outputs for denoising have the same resolution, we removed the up-sampling layer from the EDSR architecture. This layer was composed of 16 residual blocks each containing two convolutional layers and a *ReLU* nonlinear activation function. The convolution layers use 33 kernels and 256 feature channels.

The deblending module serves to decouple the lensed light and the source galaxy from the observations. This module adopts the same modified EDSR architecture that was used for the denoising module. The reason is that the source separation is also an image-to-image task that takes the images with coupled source and foreground galaxies as input and outputs the corresponding lensed

or unlensed source galaxy that is separated from the foreground lens.

The denoising and the deblending modules essentially preprocess the images in the pipeline to enhance the lens searching and modeling tasks farther down the pipeline. Performance of these modules, especially when they are used for inference, is dependent: the output of one feeds as the input to the next module. To that end, we evaluate three strategies: (1) end-to-end training, where a single model is trained such that its input is the noisy blended image and its output is the deblended image from the simulation data; (2) modular training, where the denoising and the deblending models are trained separately; and (3) joint training, where the denoising and deblending models are trained jointly by passing the output of denoising model as the input to deblending model. Here, the loss function is a weighted combination of their individual losses.

We use the L1 loss to train the denoising and the deblending models, then employ the peak signal-to-noise ratio (PSNR) to evaluate the denoising and deblending accuracy.

3.2 Lens Detection

The lens detection module is a classification module that is used to detect the lensing systems from the source separated images. In particular, each of the observed images needs to be classified as either a lensed or an unlensed system. We use the VIB approach to classification, which provides a unified framework for representation learning and predictive modeling and compared its performance with Resnet-50 model. We evaluate the classification model using the commonly used mean classification accuracy metric (mean over the two classes), area under the receiver operating characteristic curve (ROC-AUC), and precision and recall metrics. Uncertainty in the classifier predictions is quantified by using the entropy and rate metrics [3].

3.3 Lens modeling

The lens modeling module is a regression module that takes the source separated galaxy and predicts its characteristics: Einstein radius, axis ratio, and position angle. We transform the axis ratio and position angle to two components of the complex ellipticity because of the degeneracy between the axis ratio and position angle of a given lens. For instance, the combinations of $\{q, \phi\}$ and $\{1/q, \phi + \pi/2\}$ present the same morphology of an ellipsoid, which leads to unreasonable scatters in modeling GGLs with CNNs. The complex ellipticities e_1 and e_2 also avoid problems due to the periodicity of position angles.

The ability to quantify prediction uncertainty in addition to the a point estimate is critical for validation purposes, to understand the impact of error sources (degraded quality of input data due to PSF, foreground objects, atmospheric conditions, detector noise) and modeling uncertainties (insufficient size, quality and biases in the training samples, and uncertainties associated with the network). We adopt and evaluate two strategies for lens modeling: VIB and a Resnet-101 model whose last dense layer is replaced by a stochastic denseFlipout layer.

3.4 Variational Information Bottleneck

The VIB approach is a variational approximation to the information bottleneck (IB) principle [48] proposed by [4]. Considering

a joint distribution $P(X, Y)$ of the input variable X and the corresponding target variable Y , the IB principle defines an objective function that seeks to learn a latent encoding Z that is maximally expressive about Y while being maximally compressive about X . This can formally be written as

$$\min_{\theta} I(Z, Y; \theta) - \beta I(X, Z; \theta) = L, \quad (1)$$

where $I(\cdot, \cdot, \cdot)$ is the mutual information and $\beta \geq 0$ is the Lagrange multiplier that controls the trade-off between the compressiveness and the expressiveness of the model. For this reason, several studies have shown that the latent encoding using this approach leads to a better generalization capability [2, 4]. The variational approximation of this objective can be written as

$$L \geq \int dx dy dz p(x) p(y|x) p(z|x) \log q(y|z) - \beta \int dx dz p(x) p(z|x) \log \frac{p(z|x)}{r(z)}$$

$$L \geq \frac{1}{N} \sum_{n=1}^N \int dz p(z|x_n) \log q(y_n|z) - \beta p(z|x_n) \log \frac{p(z|x_n)}{r(z)}, \quad (2)$$

where $p(z|x_n)$ can be modeled by using an encoder and $q(y_n|z)$ by a decoder and $r(z)$ is the prior distribution on z . Following the standard convention of choosing a Gaussian distribution form for the encoder and standard Gaussian prior, we can end up with the familiar objective function seen with standard variational autoencoders but with an additional β factor. This objective could be maximized by using backpropagation through the reparametrization trick [25].

$$L \geq \frac{1}{N} \sum_{n=1}^N \mathbb{E}_{\epsilon \sim p(\epsilon)} - \log q(y_n|f(x_n, \epsilon)) + \beta KL[p(Z|x_n), r(Z)]. \quad (3)$$

We note that this approach combines representation learning and supervised learning in a single trainable framework and the latent space can give further insights into the model's learning process for predicting conditional distributions $P(Y|X)$, enhancing interpretability. Also, VIB is a doubly stochastic approach in the sense that both the latent variable (Z) and the target variable (Y) are treated as random variables [3] as opposed to the deterministic approaches where only the latter is treated as random variable. Hence, this approach can be used to obtain uncertainty estimates on the predictions.

For the lens detection task, the input variable X corresponds to the source separated galaxy represented as an image while the target variable Y is the binary class stating whether the image is of the lensed or the unlensed galaxy. For the lens modeling task, the input variable X corresponds to the source separated galaxy represented as an image, while the target variable Y is the three lens parameters (Einstein radius, axis ratio, and position angle). Details about the encoder and decoder architectures as well as the latent space dimensions used in this work are described in Section 4.3.

The rate metric [3] used to assess the uncertainty in the class label prediction for VIB is defined as

$$p(Y, Z|X) = \int dX p(X) p(Z|X) q(Y|Z) \approx r(Z) q(Y|Z). \quad (4)$$

In order to quantify the uncertainty in lens detection VIB model predictions, the rate metric and entropy are used.

4 Results and Discussion

The simulation model described in Section 2 provides five forms of data that were used to train the modules in the pipeline: noisy-blended galaxy images (S_1), which represent the noisy observations from the telescope; noiseless-blended galaxy images (S_2), which represent the scenario where the observed noise is perfectly removed from S_1 ; noiseless-deblended images (S_3), where the background source galaxy is perfectly separated from the foreground lensed light; data labels (S_4), which indicate whether an image in S_3 is lensed or unlensed; and lens parameters (S_5), which describe the properties of the lensed galaxies. Our goal is to train the denoising, deblending, lens detection, and lens modeling modules of the pipeline using different forms of simulation data and then use the trained models for predicting the lens parameters directly from noisy and blended galaxy images S_1 .

To evaluate the pipeline, we split the 120K images into 108K (90%) for training and use the remaining 12K images (10%) to evaluate both the training and inference modalities. We refer to the predicted outputs from the pipeline during training and inference as T_i | $i \in \{2, 3, 4, 5\}$ and I_i | $i \in \{2, 3, 4, 5\}$, respectively. The separate terminology is required in order to differentiate the predicted outputs from the modules during training and inference. A few examples of these images are shown in Figure 2.

We adapted the open source implementation of EDSR [32] written in PyTorch [38] for denoising and deblending. VIB was implemented for lens detection and lens modeling in PyTorch [38] by modifying the open source beta-tcvae implementation. The ResNet architectures for lens detection and modeling are implemented in TensorFlow [1]. All the models were trained on a single node of Tesla V100 GPU.

4.1 Denoising and deblending

Here, we compare the end-to-end, modular, and joint training strategies described in Section 3.1 and show that joint training is better than the other two.

The three strategies start with the same input S_1 . In modular and joint training, input images to the deblending module were simulated noiseless blended images (S_2) and predicted noiseless blended images (T_2), respectively. The end-to-end training does not have this stage because it takes S_1 and outputs predicted noiseless deblended images (T_3) directly. All three model were trained with the same set of hyperparameter values used in the original EDSR paper [32]. The number of epochs was set to 200. Since EDSR trains by extracting patches randomly from the full image, it can learn to perform denoising and deblending from the smaller dataset. We used a subset of 18,000 images (9,000 lensed, 9,000 unlensed), randomly selected from 108K training split to ease the computational cost of training the model.

The results show that the joint training strategy achieves higher accuracy and better stability than the modular and end-to-end training do. The modular training with different denoising and deblending models led to artifacts in the deblending model due to a discrepancy in the denoised model prediction (albeit very small). However, the joint training strategy led the deblending model to

Table 1: Accuracy metrics for training and inference. S_1, S_2, S_3 : Noisy blended, noiseless blended, and noiseless deblended simulation data; S_4 : Data labels that indicate whether S_3 is lensed or unlensed; S_5 : Lens parameters that describe the properties of the lensed galaxies; T_2, T_3 : output from the denoising and deblending module respectively in the training modality; T_4, I_4 : data labels predicted by the lens detection module in the training and inference modality respectively; T_5, I_5 : Lens parameters predicted by the lens modeling module in the training and inference modality respectively.

(a) PSNR metrics for denoising and deblending on 12000 test split images (the training and inference modality is same in this case because we adopted the joint training strategy for denoising and deblending).

Train/Infer Modality	PSNR
Denoising	
S_1 vs. S_2	22.89
S_2 vs. T_2	45.66
Deblending	
S_2 vs. S_3	13.63
S_3 vs. T_3	32.69

(b) Training and Inference - Classification metrics on 12000 test split images

Training Modality	Mean acc	AU-ROC	Prec, Rec
T_4 (using S_1) vs. S_4 (ResNet50)	0.82	0.81	0.78, 0.74
T_4 vs. S_4 (ResNet50)	0.99	0.99	0.99, 0.99
T_4 vs. S_4 (VIB)	0.99	0.99	0.99, 0.99
Inference Modality			
I_4 vs. S_4 (ResNet50)	0.93	0.96	0.93, 0.92
I_4 vs. S_4 (VIB)	0.94	0.97	0.94, 0.93

(c) Training and Inference - Accuracy metrics on 6000 lensed subset of test split images

Baseline	MAE-ResNet101	
T_5 (using S_1) vs. S_5	0.08	-
Training Modality	MAE-VIB	MAE-R101+DF
T_5 vs. S_5	0.01	0.09
Inference Modality	MAE-VIB	MAE-R101+DF
I_5 vs. S_5	0.06	0.11

become robust to this discrepancy. For the end-to-end training strategy, the model quickly diverged, and its prediction results were poor. A few sample outputs from the denoising and deblending model are shown in Fig. 2

The accuracy metrics for the joint training strategy are shown in Table 1a. In the case of denoising, we first calculate the PSNR value of the difference between S_1 and S_2 , whose mean value across the test data split is 22.89. The low value of PSNR demonstrates the significant difference between the noisy and noiseless simulation data. This motivates the need for training a model to remove this noise. To this end, we compared the denoising model prediction (T_2) with the same ground truth (S_2) on the test data split and found

the PSNR value to be 45.66. This demonstrates that the denoising model has learned to remove the noise.

Similarly, for the deblending case, we compared S_2 with S_3 , whose mean value on the test data split is seen to be 13.63. The low PSNR value indicates a significant difference between the blended and the deblended images, which is expected since the latter contains only the background galaxy in the image. We also compared the deblending module prediction (T_3) with the same ground truth (S_3) and found the PSNR value on the test data split to be 32.69. This indicates a good recovery of the source galaxy by deblending.

Since we adopted the joint training strategy for denoising and deblending, where the output of the denoising module is used as input to the deblending module, both the training and the inference modalities are equivalent in this case.

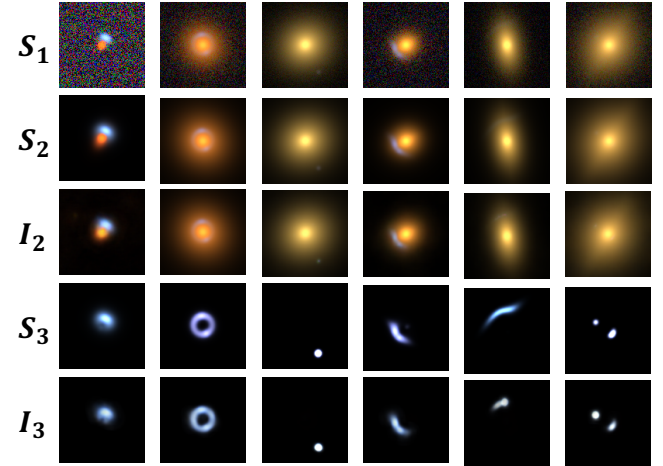


Figure 2: First row: noisy blended data from the simulation (S_1); Second row: noiseless blended simulation data (S_2); Third row: output from the denoising module at inference (I_2); Fourth row: noiseless deblended simulation data (S_3); Fifth row: output from the deblending model (I_3);

4.2 Lens Detection

We adopted the VIB approach described in Section 3.3 for lens detection. The encoder in the VIB model consists of 6 convolutional layers with batch normalization between each of the layers, with the output from the last layer corresponding to twice the latent dimension (to model the mean and standard deviation) of the latent space, which is modeled as a 10-dimensional Gaussian distribution. We used factorial normalizing flow (FNF) on top of this as a flexible prior, where each dimension is a normalizing flow of depth 32. The FNF can fit multimodal distributions, and so it is ideal for the classification module. The decoder, on the other hand, consists of four fully connected neural network layers that takes a 10-dimensional input from the latent space to a Bernoulli distribution with a logits parameterization for the binary class prediction. The hyperparameters in the model closely follow those in [10] (learning rate of $1e-3$ and batch size of 2048, as we adopted the weighted minibatches approach) except that the number of epochs and β terms were set to 300 and 0.5, respectively, based on an empirical study. A thorough hyperparameter search will be considered in future work.

As a comparison, we also trained a ResNet50 model with a batch size of 512 (the maximum batch size that we could fit in Tesla V100 GPU memory) and 150 epochs (since we saw that the model converged and was not improving) with rest of the hyperparameters matching the VIB model.

Both these models were trained over the 108K image training data and tested on rest of 12K image test data. The mean classification accuracy (over two classes) as well as AU-ROC, precision, and recall metrics were used to measure the accuracy of the classification model (Table 1b). As a baseline, we trained a ResNet50 model to predict the label directly from the noisy blended simulation images (S_1), and we evaluated the metrics on the same test data. The mean accuracy was 0.82. The model trained with S_3 as input gave a mean accuracy of 0.99 with ResNet50 and 0.99 with VIB and, for the two models, AU-ROC of 0.99 and precision and recall of 0.99 and 0.99, respectively, showing a significant improvement over the baseline.

For inference, the lens detection module was fed the output from the deblending module I_3 as input to predict I_4 . We obtained a mean accuracy of 0.93 with ResNet50 and 0.94 with VIB and, for the two models, AU-ROC of 0.96 and 0.97, precision of 0.93 and 0.94, and recall of 0.92 and 0.93, respectively.

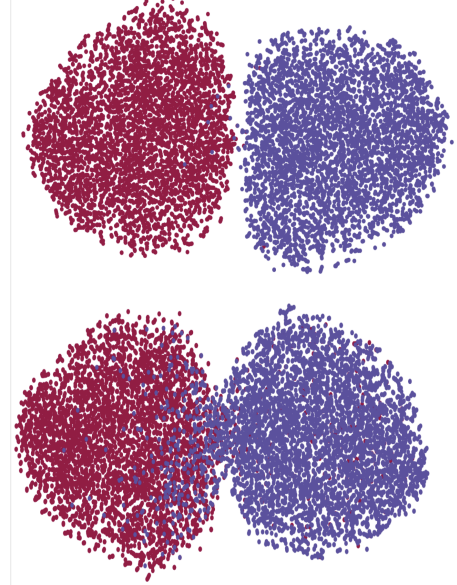
The VIB model provides additional insights into the decision-making of the model by visualizing the latent space and calculating the uncertainty metrics of entropy and rate. Figure 3(a) shows the latent space for 12K test data split of S_3 images used as input to the model on the top and I_3 input on the bottom. A clear separation exists between the two classes in the latent space for S_3 ; but for I_3 , the misclassified ones are at the intersection of the modes. To ascertain the reason for this misclassification, we calculated the rate metric and found that for the left mode the images falsely classified as lensed in fact correspond to low values of rate, showing higher uncertainty in the model predictions. Further inspection revealed that these points correspond to low magnification and low signal-to-noise ratio; which are difficult for the deblending model to predict. The entropy metric shows that the model is more uncertain about the images, which it considers as between the two classes. These results confirm our intuition, but the rate metric provides better insights.

4.3 Lens modeling

For the lens modeling, we again used the VIB approach. Only the lensed images in the deblended simulation data S_3 were used to train the regression model. Hence, a total of 54,000 were used for training and 6,000 for testing. The encoder and decoder in the VIB model for lens modeling were similar to those used for lens detection except that the decoder outputs a three-dimensional vector to predict the lens parameters with the likelihood chosen to be a Gaussian distribution. Similar to the lens detection VIB model, the hyperparameters closely follow those in [10] except that the number of epochs and β terms were set to 300 and 3, respectively, based on an empirical study. A thorough hyperparameter search will be considered in future work.

For comparison, we used an additional architecture for the regression module where we implemented a Resnet-101 model for parameter estimation but with a densely connected layer class with

(a) Latent space comparison for the test data split in training and inference modality. Clear separation exists between the two classes in the latent space for the former while the misclassified data are at the intersection of the modes for the latter.



(b) Rate metric for inference modality. The misclassified lensed data correspond to low rate value and hence high uncertainty.

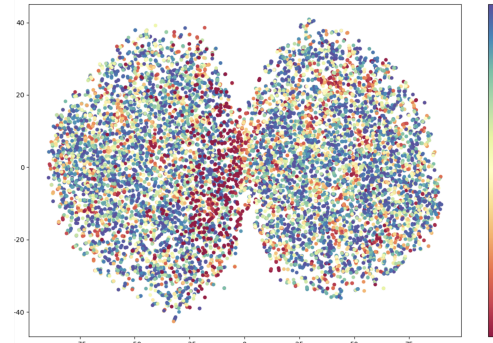


Figure 3: Vizualization of the latent space for the lens detection VIB model.

Flipout estimator [51]. As a baseline, we trained a deterministic ResNet101 model to predict the lens parameters directly from the noisy blended simulation images (S_1), and we evaluated the metrics on the same test data split. All of them were trained with same hyperparameters as VIB except that the batch size was 512 (the maximum batch size that we could fit in Tesla V100 GPU memory).

The regression accuracy was measured by using the mean absolute error (MAE) in the normalized ($[0,1]$ w.r.t the maximum and minimum of training data) coordinates, as shown in Table 1c. The plots comparing the observed and predicted are shown in Fig. 6. The MAE on the test data split for training modality using the VIB model was 0.01, which indicates very good agreement with the ground truth. The corresponding accuracy for the ResNet-101 with the Flipout estimator was much lower (MAE = 0.09). This result indicates a superior performance with the VIB model. The baseline

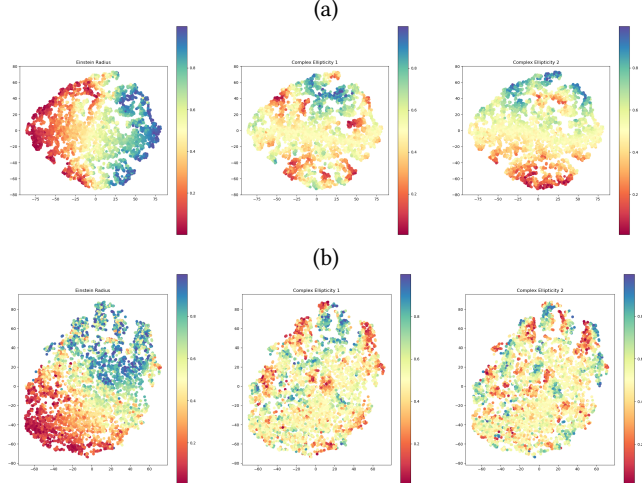


Figure 4: Visualization of latent space (a) with the corresponding regression outputs of the VIB model and (b) reconstructing the input images.

model trained on the S_1 data also had a much lower MAE (0.08) on the test data split.

To gain additional insights into the VIB model, we visualized its latent space. Figure 5 shows a 2D t-SNE projection of the 10-dimensional latent space where every sample of the latent space is labeled with the corresponding input image. The trend in the data can be analyzed by visualizing the characteristics of the images close together in this projected space. We can see that similarly shaped lenses are grouped together with the solid dots on the far left; these gradually change to hollow circles as we move right, and they change to arcs as we move to the bottom. To make a quantitative analysis, we colored the latent samples with the value of the target variable (three in our case) as seen in 4(a). The results show that the projection of the latent space admits a gradual change in the Einstein radius from left to right and one of complex ellipticity from bottom to top. The ability to obtain a good latent representation amenable to the regression task is a particularly important feature of the VIB model, enabling the model to obtain good regression accuracy albeit with a shallower network and less training time. In Fig 4(b) we show a similar 2D projection of the 10-dimensional latent space obtained when we reconstruct the input image instead of predicting the lens parameters (a common exercise for representation learning using generative models). We see that although the gradual change in Einstein radius is admitted in the latent space, the other two variables have no trend. These results highlight an important point about the need to custom train the latent space for a given task in order to make the best use of the model. We obtain the uncertainty bounds on the model prediction through Monte Carlo sampling of the latent space posterior illustrated in Figure 6.

For the inference modality, we found that the regression accuracy on the 6000 images is slightly lower (MAE of 0.06) than the accuracies obtained with the training modality but is an improvement over the baseline of 0.08. The Resnet101 model with the dense Flipout layer has a lower regression accuracy with MAE of 0.11.

5 Conclusions

The combination of high-fidelity simulation data and a systematic machine learning pipeline is crucial for developing fast and accurate GGSL analysis techniques for future cosmological surveys. To this end, we generated a dataset of 120,000 synthetic images (60,000 GGSLs and 60,000 non-GGSLs), which we utilized to develop a deep learning pipeline with separate modules for denoising, deblending, lens detection, and modeling. The modular nature of our pipeline allowed us to train, test, and evaluate each component in isolation and helped us understand their efficacy.

We adopted the EDSR model for denoising and deblending modules that provided a good recovery (PSNR of 45.66 and 32.69, respectively) of the ground truth for both modules trained on the simulated data. For lens detection and lens modeling we adopted the variational information bottleneck (VIB) approach that provides superior accuracy (12% improvement for lens detection and 25% for lens modeling) over the baseline and other deep ResNet architectures with only a small fraction of layers. In addition, the VIB model provides model interpretability by visualizing the latent space. The lens detection model produces a latent space that perfectly separates the two classes, thus demonstrating a good representation learning capability when tested on the simulation inputs. With the inference pipeline, the higher uncertainty images (according to the rate metric) correspond to the misclassified images, which in turn belong to the low-magnification, low signal-to-noise ratio region that is known to have difficulty in deblending. For lens modeling, we find that the learned latent space has more semantic meaning than that learned with unsupervised methods such as the variational autoencoder. We therefore conclude that a latent space customized for a supervised learning task is better suited than unsupervised or generic representation.

We also identified limitations of the mock data, which are relatively simple models of mass and light profiles of lens and source galaxies used in the simulation. The choices lead to underestimated contamination from substructures in the context of both mass and light distributions of galaxies in the cutouts, in turn leading to either miscounted images or introduce additional artifacts in the procedures of all modules. The issue is hardly noticeable in the data of ground-based surveys because of the large pixel size and spread of the PSF. It becomes significant, however, in the data of space-based surveys with much higher spatial resolutions. To widen the scope of our pipeline, we plan to employ more realistic mass and light models as well as create a larger image dataset. Eventually, we intend to utilize the pipeline for real-time lens detection and modeling with data from next-generation large-scale sky surveys, including both ground- and space-based telescopes such as Euclid, LSST, and WFIRST,³ where fast and automated methods of detecting and characterizing astronomical objects become a necessity.

References

- [1] Martin Abadi, Paul Barham, Jianmin Chen, Zhifeng Chen, Andy Davis, Jeffrey Dean, Matthieu Devin, Sanjay Ghemawat, Geoffrey Irving, Michael Isard, et al. 2016. TensorFlow: A system for large-scale machine learning. In *12th {USENIX} Symposium on Operating Systems Design and Implementation ({OSDI} 16)*. 265–283.
- [2] Alessandro Achille and Stefano Soatto. 2018. Emergence of invariance and disentanglement in deep representations. *The Journal of Machine Learning*

³ <https://wfirst.gsfc.nasa.gov/>

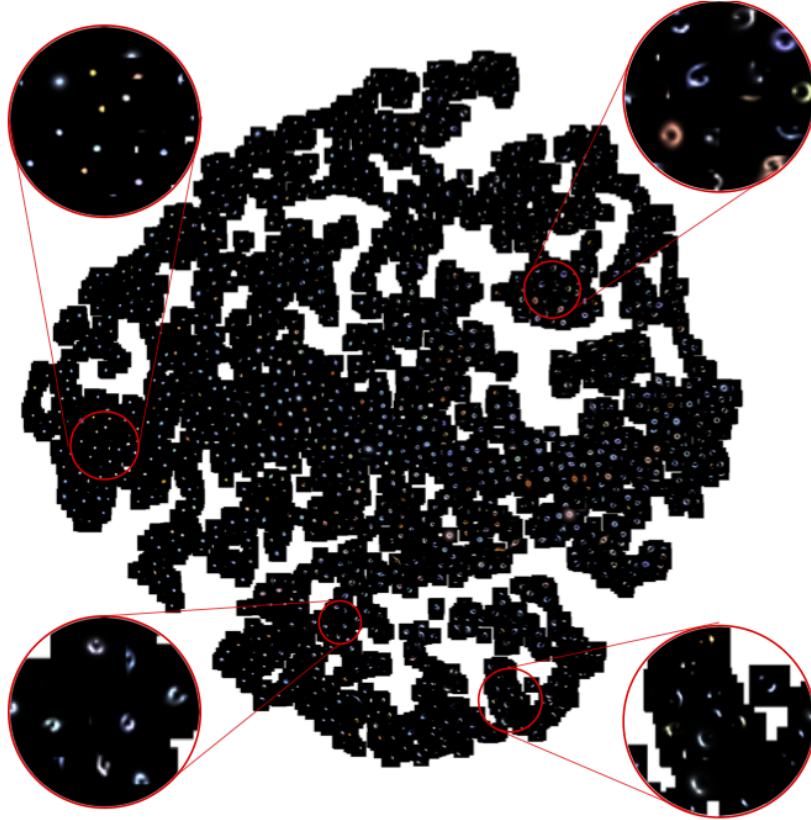


Figure 5: Visualization of latent space with the corresponding input images in VIB regression. Four zoomed-in panels show qualitatively different types of strong lenses.

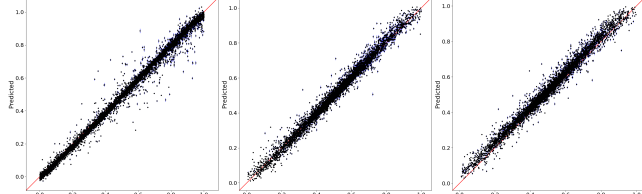


Figure 6: Comparison of the observed (S_5) and predicted (T_5) data (and the error bars of one standard deviation) corresponding to testing data for lens modeling (regression) in the training modality using VIB.

Research 19, 1 (2018), 1947–1980.

- [3] Alexander A Alemi, Ian Fischer, and Joshua V Dillon. 2018. Uncertainty in the variational information bottleneck. *arXiv preprint arXiv:1807.00906* (2018).
- [4] Alexander A Alemi, Ian Fischer, Joshua V Dillon, and Kevin Murphy. 2016. Deep variational information bottleneck. *arXiv preprint arXiv:1612.00410* (2016).
- [5] Saeed Anwar, Salman Khan, and Nick Barnes. 2019. A Deep Journey into Super-resolution: A survey. *arXiv preprint arXiv:1904.07523* (2019).
- [6] C. Avestruz, N. Li, H. Zhu, M. Lightman, T. E. Collett, and W. Luo. 2019. Automated Lensing Learner: Automated Strong Lensing Identification with a Computer Vision Technique. *ApJ 877*, Article 58 (May 2019), 58 pages. <https://doi.org/10.3847/1538-4357/ab16d9> *arXiv:astro-ph.IM/1704.02322*
- [7] D. Bayer, S. Chatterjee, L. V. E. Koopmans, S. Vegetti, J. P. McKean, T. Treu, and C. D. Fassnacht. 2018. Observational constraints on the sub-galactic matter-power spectrum from galaxy-galaxy strong gravitational lensing. *ArXiv e-prints* (March 2018). *arXiv:1803.05952*
- [8] M. B. Bayliss, K. Sharon, A. Acharyya, M. D. Gladders, J. R. Rigby, F. Bian, R. Bordoloi, J. Runnoe, H. Dahle, L. Kewley, M. Florian, T. Johnson, and R. Paterno-Mahler. 2017. Spatially Resolved Patchy Ly α Emission within the Central Kiloparsec of a Strongly Lensed Quasar Host Galaxy at $z = 2.8$. *ApJ 845*, Article L14 (Aug. 2017), L14 pages. <https://doi.org/10.3847/2041-8213/aa831a> *arXiv:1708.00453*
- [9] C. R. Bom, M. Makler, M. P. Albuquerque, and C. H. Brandt. 2017. A neural network gravitational arc finder based on the Mediatrix filamentation method. *A&A 597*, Article A135 (Jan. 2017), A135 pages. <https://doi.org/10.1051/0004-6361/201629159> *arXiv:1607.04644*
- [10] Tian Qi Chen, Xuechen Li, Roger B Grosse, and David K Duvenaud. 2018. Isolating Sources of Disentanglement in Variational Autoencoders. In *Advances in Neural Information Processing Systems*. 2610–2620.
- [11] T. E. Collett. 2015. The Population of Galaxy-Galaxy Strong Lenses in Forthcoming Optical Imaging Surveys. *ApJ 811*, Article 20 (Sept. 2015), 20 pages. <https://doi.org/10.1088/0004-637X/811/1/20> *arXiv:1507.02657*
- [12] T. E. Collett and M. W. Auger. 2014. Cosmological constraints from the double source plane lens SDSSJ0946+1006. *MNRAS 443* (Sept. 2014), 969–976. <https://doi.org/10.1093/mnras/stu1190> *arXiv:1403.5278*
- [13] A. J. Connolly, John Peterson, J. Garrett Jernigan, Robert Abel, Justin Bankert, Chihway Chang, Charles F. Claver, Robert Gibson, David K. Gilmore, Emily Grace, R. Lynne Jones, Zeljko Ivezic, James Jee, Mario Juric, Steven M. Kahn, Victor L. Krabbendam, Simon Krughoff, Suzanne Lorenz, James Pizagno, Andrew Rasmussen, Nathan Todd, J. Anthony Tyson, and Mallory Young. 2010. Simulating the LSST system. *SPIE 7738* (2010). <https://doi.org/10.1117/12.857819>
- [14] S. Dye, N. W. Evans, V. Belokurov, S. J. Warren, and P. Hewett. 2008. Models of the Cosmic Horseshoe gravitational lens J1004+4112. *MNRAS 388*, 1 (Jul 2008), 384–392. <https://doi.org/10.1111/j.1365-2966.2008.13401.x> *arXiv:astro-ph/0804.4002*
- [15] S. Dye, C. Furlanetto, L. Dunne, S. A. Eales, M. Negrello, H. Nayyeri, P. P. van der Werf, S. Serjeant, D. Farrah, M. J. Michałowski, M. Baes, L. Marchetti, A. Cooray, D. A. Riechers, and A. Amvrosiadis. 2018. Modelling high-resolution ALMA observations of strongly lensed highly star-forming galaxies detected by Herschel. *MNRAS 476* (2018), 4383–4394. <https://doi.org/10.1093/mnras/sty513>
- [16] R. Gavazzi, P. J. Marshall, T. Treu, and A. Sonnenfeld. 2014. RINGFINDER: Automated Detection of Galaxy-scale Gravitational Lenses in Ground-based

A Modular Deep Learning Pipeline for Galaxy-Scale Strong Gravitational Lens Detection and Modeling

Multi-filter Imaging Data. *ApJ* 785, Article 144 (April 2014), 144 pages. <https://doi.org/10.1088/0004-637X/785/2/144> arXiv:1403.1041

[17] Raphaël Gavazzi, Tommaso Treu, Jason D. Rhodes, Léon V. E. Koopmans, Adam S. Bolton, Scott Burles, Richard J. Massey, and Leonidas A. Moustakas. 2007. The Sloan Lens ACS Survey, IV: The Mass Density Profile of Early-Type Galaxies out to 100 Effective Radii. *ApJ* 667, 1 (Sep 2007), 176–190. <https://doi.org/10.1086/519237> arXiv:astro-ph/astro-ph/0701589

[18] D. Gilman, S. Birrer, T. Treu, and C. R. Keeton. 2017. Probing the nature of dark matter by forward modeling flux ratios in strong gravitational lenses. *ArXiv e-prints* (Dec. 2017). arXiv:1712.04945

[19] P. Hartley, R. Flamary, N. Jackson, A. S. Tagore, and R. B. Metcalf. 2017. Support vector machine classification of strong gravitational lenses. *MNRAS* 471 (Nov. 2017), 3378–3397. <https://doi.org/10.1093/mnras/stx1733> arXiv:astro-ph.IM/1705.08949

[20] J. N. Hewitt, E. L. Turner, D. P. Schneider, B. F. Burke, and G. I. Langston. 1988. Unusual radio source MG1131+0456 - A possible Einstein ring. *Nature* 333 (June 1988), 537–540. <https://doi.org/10.1038/333537a0>

[21] Y. D. Hezaveh, N. Dalal, D. P. Marrone, Y.-Y. Mao, W. Morningstar, D. Wen, R. D. Blandford, J. E. Carlstrom, C. D. Fassnacht, G. P. Holder, A. Kemball, P. J. Marshall, N. Murray, L. Perreault Levasseur, J. D. Vieira, and R. H. Wechsler. 2016. Detection of Lensing Substructure Using ALMA observations of the Dusty Galaxy SDP.81. *ApJ* 823, Article 37 (May 2016), 37 pages. <https://doi.org/10.3847/0004-637X/823/1/37> arXiv:1601.01388

[22] Yashar D. Hezaveh, Laurence Perreault Levasseur, and Philip J. Marshall. 2017. Fast automated analysis of strong gravitational lenses with convolutional neural networks. *Nature* 548, 7669 (Aug 2017), 555–557. <https://doi.org/10.1038/nature23463> arXiv:astro-ph.IM/1708.08842

[23] C. Jacobs, K. Glazebrook, T. Collett, A. More, and C. McCarthy. 2017. Finding strong lenses in CFHTLS using convolutional neural networks. *MNRAS* 471 (Oct. 2017), 167–181. <https://doi.org/10.1093/mnras/stx1492> arXiv:astro-ph.IM/1704.02744

[24] R. Joseph, F. Courbin, R. B. Metcalf, C. Giocoli, P. Hartley, N. Jackson, F. Bellagamba, J.-P. Kneib, L. Koopmans, G. Lemson, M. Meneghetti, G. Meylan, M. Petkova, and S. Pires. 2014. A PCA-based automated finder for galaxy-scale strong lenses. *A&A* 566, Article A63 (June 2014), A63 pages. <https://doi.org/10.1051/0004-6361/201423365> arXiv:astro-ph.IM/1403.1063

[25] Diederik P Kingma and Max Welling. 2013. Auto-encoding variational Bayes. *arXiv preprint arXiv:1312.6114* (2013).

[26] Léon V. E. Koopmans, Tommaso Treu, Adam S. Bolton, Scott Burles, and Leonidas A. Moustakas. 2006. The Sloan Lens ACS Survey, III: The Structure and Formation of Early-Type Galaxies and Their Evolution since $z=1$. *ApJ* 649, 2 (Oct 2006), 599–615. <https://doi.org/10.1086/505969> arXiv:astro-ph/astro-ph/0601628

[27] Danila Korytov, Andrew Hearn, Eve Kovacs, Patricia Larsen, Esteban Rangel, Joseph Hollowed, Andrew J. Benson, Katrin Heitmann, Yao-Yuan Mao, Anita Bahmanyar, Chihway Chang, Duncan Campbell, Joseph Derose, Hal Finkel, Nicholas Frontiere, Eric Gawiser, Salman Habib, Benjamin Joachimi, François Lanusse, Nan Li, Rachel Mandelbaum, Christopher Morrison, Jeffrey A. Newman, Adrian Pope, Eli Rykoff, Melanie Simei, Chun-Hao To, Vini Vikraman, Risa H. Wechsler, and Martin White. 2019. CosmoDC2: A Synthetic Sky Catalog for Dark Energy Science with LSST. *ArXiv e-prints*, Article arXiv:1907.06530 (Jul 2019), arXiv:1907.06530 pages. arXiv:astro-ph.CO/1907.06530

[28] J. Kummer, F. Kahlhoefer, and K. Schmidt-Hoberg. 2018. Effective description of dark matter self-interactions in small dark matter haloes. *MNRAS* 474 (Feb. 2018), 388–399. <https://doi.org/10.1093/mnras/stx2715> arXiv:1706.04794

[29] R. Küng, P. Saha, I. Ferreras, E. Baeten, J. Coles, C. Cornen, C. Macmillan, P. Marshall, A. More, L. Oswald, A. Verma, and J. K. Wilcox. 2018. Models of gravitational lens candidates from Space Warps CFHTLS. *MNRAS* 474 (March 2018), 3700–3713. <https://doi.org/10.1093/mnras/stx3012> arXiv:1711.07297

[30] F. Lanusse, Q. Ma, N. Li, T. E. Collett, C.-L. Li, S. Ravanbakhsh, R. Mandelbaum, and B. Póczos. 2018. CMU DeepLens: deep learning for automatic image-based galaxy-galaxy strong lens finding. *MNRAS* 473 (Jan. 2018), 3895–3906. <https://doi.org/10.1093/mnras/stx1665> arXiv:astro-ph.IM/1703.02642

[31] Nan Li, Michael D. Gladders, Esteban M. Rangel, Michael K. Florian, Lindsey E. Bleem, Katrin Heitmann, Salman Habib, and Patricia Fasel. 2016. PICS: Simulations of Strong Gravitational Lensing in Galaxy Clusters. *ApJ* 828, 1, Article 54 (Sep 2016), 54 pages. <https://doi.org/10.3847/0004-637X/828/1/54> arXiv:astro-ph.CO/1511.03673

[32] Bee Lim, Sanghyun Son, Heewon Kim, Seungjun Nah, and Kyoung Mu Lee. 2017. Enhanced deep residual networks for single image super-resolution. In *Proceedings of the IEEE Conference on Computer Vision and Pattern Recognition Workshops*. 136–144.

[33] R. B. Metcalf, M. Meneghetti, C. Avestruz, F. Bellagamba, C. R. Bom, E. Bertin, R. Cabanac, F. Courbin, A. Davies, E. Decencière, R. Flamary, R. Gavazzi, M. Geiger, P. Hartley, M. Huertas-Company, N. Jackson, C. Jacobs, E. Jullo, J.-P. Kneib, L. V. E. Koopmans, F. Lanusse, C.-L. Li, Q. Ma, M. Makler, N. Li, M. Lightman, C. E. Petrillo, S. Serjeant, C. Schäfer, A. Sonnenfeld, A. Tagore, C. Tortora, D. Tuccillo, M. B. Valentín, S. Velasco-Forero, G. A. Verdoes Kleijn, and G. Vernardos. 2019. The strong gravitational lens finding challenge. *A&A* 625, Article A119 (May 2019), A119 pages. <https://doi.org/10.1051/0004-6361/201832797> arXiv:1802.03609

[34] Warren R. Morningstar, Yashar D. Hezaveh, Laurence Perreault Levasseur, Roger D. Blandford, Philip J. Marshall, Patrick Putzky, and Risa H. Wechsler. 2018. Analyzing interferometric observations of strong gravitational lenses with recurrent and convolutional neural networks. *arXiv e-prints*, Article arXiv:1808.00011 (Jul 2018), arXiv:1808.00011 pages. arXiv:astro-ph.IM/1808.00011

[35] Warren R. Morningstar, Laurence Perreault Levasseur, Yashar D. Hezaveh, Roger Blandford, Phil Marshall, Patrick Putzky, Thomas D. Rueter, Risa Wechsler, and Max Welling. 2019. Data-driven Reconstruction of Gravitationally Lensed Galaxies Using Recurrent Inference Machines. *ApJ* 883, 1, Article 14 (Sep 2019), 14 pages. <https://doi.org/10.3847/1538-4357/ab35d7> arXiv:astro-ph.IM/1901.01359

[36] F. Ostromski, R. G. McMahon, A. J. Connolly, C. A. Lemon, M. W. Auger, M. Banerji, J. M. Hung, S. E. Koposov, C. E. Lidman, S. L. Reed, S. Allam, A. Benoit-Lévy, E. Bertin, D. Brooks, E. Buckley-Geer, A. Carnero Rosell, M. Carrasco Kind, J. Carretero, C. E. Cunha, L. N. da Costa, S. Desai, H. T. Diehl, J. P. Dietrich, A. E. Evrard, D. A. Finley, B. Flaugher, P. Fosalba, J. Frieman, D. W. Gerdes, D. A. Goldstein, D. Gruen, R. A. Gruendl, G. Gutierrez, K. Honscheid, D. J. James, K. Kuehn, N. Kuropatkin, M. Lima, H. Lin, M. A. G. Maia, J. L. Marshall, P. Martini, P. Melchior, R. Miquel, R. Ogando, A. Plazas Malagón, K. Reil, K. Romer, E. Sanchez, B. Santiago, V. Scarpine, I. Sevilla-Noarbe, M. Soares-Santos, F. Sobreira, E. Suchyta, G. Tarle, D. Thomas, D. L. Tucker, and A. R. Walker. 2017. VDES J2325-5229 a $z=2.7$ gravitationally lensed quasar discovered using morphology-independent supervised machine learning. *MNRAS* 465 (March 2017), 4325–4334. <https://doi.org/10.1093/mnras/stw2958> arXiv:1607.01391

[37] D. Paraficz, F. Courbin, A. Tramacere, R. Joseph, R. B. Metcalf, J.-P. Kneib, P. Dubath, D. Droz, F. Filleul, D. Ringeisen, and C. Schäfer. 2016. The PCA Lens-Finder: application to CFHTLS. *A&A* 592, Article A75 (July 2016), A75 pages. <https://doi.org/10.1051/0004-6361/201527971> arXiv:1605.04309

[38] Adam Paszke, Sam Gross, Soumith Chintala, Gregory Chanan, Edward Yang, Zachary DeVito, Zeming Lin, Alban Desmaison, Luca Antiga, and Adam Lerer. 2017. Automatic Differentiation in PyTorch. (2017).

[39] J. Pearson, N. Li, and S. Dye. 2019. The use of convolutional neural networks for modelling large optically-selected strong galaxy-lens samples. *MNRAS* 488 (Sept. 2019), 991–1004. <https://doi.org/10.1093/mnras/stz1750> arXiv:astro-ph.IM/1904.06199

[40] L. Perreault Levasseur, Y. D. Hezaveh, and R. H. Wechsler. 2017. Uncertainties in Parameters Estimated with Neural Networks: Application to Strong Gravitational Lensing. *ApJ* 850, Article L7 (Nov. 2017), L7 pages. <https://doi.org/10.3847/2041-8213/aa9704> arXiv:1708.08843

[41] C. E. Petrillo, C. Tortora, S. Chatterjee, G. Vernardos, L. V. E. Koopmans, G. Verdoes Kleijn, N. R. Napolitano, G. Covone, P. Schneider, A. Grado, and J. McFarland. 2017. Finding strong gravitational lenses in the Kilo Degree Survey with Convolutional Neural Networks. *MNRAS* 472, 1 (Nov 2017), 1129–1150. <https://doi.org/10.1093/mnras/stx2052> arXiv:astro-ph.GA/1702.07675

[42] A. Rana, D. Jain, S. Mahajan, A. Mukherjee, and R. F. L. Holanda. 2017. Probing the cosmic distance duality relation using time delay lenses. *J. Cosmology Astropart. Phys.* 7, Article 010 (July 2017), 010 pages. <https://doi.org/10.1088/1475-7516/2017/07/010> arXiv:1705.04549

[43] P. Sharda, C. Federrath, E. daÂ Cunha, A. M. Swinbank, and S. Dye. 2018. Testing star formation laws in a starburst galaxy at redshift 3 resolved with ALMA. *MNRAS* 477 (July 2018), 4380–4390. <https://doi.org/10.1093/mnras/sty886> arXiv:1712.03661

[44] Y. Shu, A. S. Bolton, S. Mao, C. S. Kochanek, I. Pérez-Fournon, M. Oguri, A. D. Montero-Dorta, M. A. Cornachione, R. Marques-Chaves, Z. Zheng, J. R. Brownstein, and B. Ménard. 2016. The BOSS Emission-line Lens Survey, IV: Smooth lens models for the BELLS GALLERY sample. *ApJ* 833, Article 264 (Dec. 2016), 264 pages. <https://doi.org/10.3847/1538-4357/833/2/264> arXiv:1608.08707

[45] Y. Shu, A. S. Bolton, L. A. Moustakas, D. Stern, A. Dey, J. R. Brownstein, S. Burles, and H. Spinrad. 2016. Kiloparsec Mass/Light Offsets in the Galaxy Pair- $\text{Ly}\alpha$ Emitter Lens System SDSS J1011+0143. *ApJ* 820, Article 43 (March 2016), 43 pages. <https://doi.org/10.3847/0004-637X/820/1/43> arXiv:1602.02927

[46] A. Sonnenfeld, T. Treu, P. J. Marshall, S. H. Suyu, R. Gavazzi, M. W. Auger, and C. Nipoti. 2015. The SL2S Galaxy-scale Lens Sample, V: Dark Matter Halos and Stellar IMF of Massive Early-type Galaxies Out to Redshift 0.8. *ApJ* 800, Article 94 (Feb. 2015), 94 pages. <https://doi.org/10.1088/0004-637X/800/2/94> arXiv:1410.1881

[47] S. H. Suyu, V. Bonvin, F. Courbin, C. D. Fassnacht, C. E. Rusu, D. Sluse, T. Treu, K. C. Wong, M. W. Auger, X. Ding, S. Hilbert, P. J. Marshall, N. Rumbaugh, A. Sonnenfeld, M. Tewes, O. Tihhonova, A. Agnello, R. D. Blandford, G. C.-F. Chen, T. Collett, L. V. E. Koopmans, K. Liao, G. Meylan, and C. Spinelli. 2017. H0LiCOW - I: H_0 lenses in COSMOGRAIL's Wellspring: program overview. *MNRAS* 468 (July 2017), 2590–2604. <https://doi.org/10.1093/mnras/stx483> arXiv:1607.00017

[48] Naftali Tishby, Fernando C Pereira, and William Bialek. 2000. The information bottleneck method. *arXiv preprint physics/0004057* (2000).

[49] Tommaso Treu. 2010. Strong Lensing by Galaxies. *ARA&A* 48 (Sep 2010), 87–125. <https://doi.org/10.1146/annurev-astro-081309-130924> arXiv:astro-ph.CO/1003.5567

- [50] S. Vegetti, L. V. E. Koopmans, M. W. Auger, T. Treu, and A. S. Bolton. 2014. Inference of the cold dark matter substructure mass function at $z = 0.2$ using strong gravitational lenses. *MNRAS* 442 (Aug. 2014), 2017–2035. <https://doi.org/10.1093/mnras/stu943> arXiv:1405.3666
- [51] Yeming Wen, Paul Vicol, Jimmy Ba, Dustin Tran, and Roger Grosse. 2018. Flipout: Efficient pseudo-independent weight perturbations on mini-batches. *arXiv preprint arXiv:1803.04386* (2018).
- [52] Abdellatif Zaidi, Iñaki Estella-Aguerri, et al. 2020. On the Information Bottleneck Problems: Models, Connections, Applications and Information Theoretic Views. *Entropy* 22, 2 (2020), 151.
- [53] Yulun Zhang, Yapeng Tian, Yu Kong, Bineng Zhong, and Yun Fu. 2018. Residual dense network for image super-resolution. In *Proceedings of the IEEE Conference on Computer Vision and Pattern Recognition*. 2472–2481.